Germanium-doped hydroxyapatite: Synthesis and characterization of a new substituted apatite

Vuk Uskoković [a,b,*], Nenad Ignjatović [c], Srečo Škapin [d], Dragan P. Uskoković [c]

[a] Advanced Materials and Nanobiotechnology Laboratory, TardigradeNano LLC, Irvine, CA, 92604, USA
[b] Department of Mechanical Engineering, San Diego State University, San Diego, CA, 92182, USA
[c] Institute of Technical Sciences of the Serbian Academy of Sciences and Arts, Belgrade, Serbia
[d] Advanced Materials Department, Jožef Stefan Institute, Ljubljana, Slovenia

ARTICLE INFO

ABSTRACT

Hydroxyapatite (HAp) is the major component of all boney tissues in mammals. Because of this omnipresence in the living world, HAp possesses an exceptional biocompatibility. The downside of this omnipresence, however, comes in the form of its mild to moderate biological activities. One means of augmenting these activities involves the doping of HAp with foreign ions. Here, the first synthesis and characterization of HAp doped with germanium ions is being reported. Germanium was deliberately integrated into the crystal lattice of HAp in the form of germanate anions. Approximately two thirds of the germanate ions introduced into the hydrothermal solution got incorporated into the HAp lattice, yielding the approximate stoichiometry of $Ca_{10-x}(PO_4)_{5.62+y}(GeO_3)_{0.38}(OH)_{2-z}$. Germanates replaced the phosphates of stoichiometric HAp and induced the expansion of the HAp lattice both along the screw axis of the calcium ion hexagons and in the direction parallel to the basal plane. Simultaneously, the larger size and the triple valency of the germanate ion as compared to the smaller and trivalent phosphates prompted the bond distortion and charge compensation through defect formation, which reduced the crystallinity and increased the microstrain of the HAp lattice. Vibrational spectroscopic analyses corroborated these crystallographic effects by demonstrating the enhanced heterogeneity of the environments surrounding the active modes after germanate ions were incorporated into HAp. Conforming to La Châtelier's principle, this reduction of the crystallographic order increased the capacity of the material for integration of adventitious carbonates. However, the inclusion of germanate ions induced a partial shift of these carbonates to the hydroxyl channel sites, thus decreasing the ratio of the B-type carbonation to the A-type carbonation. Introduced into HAp, germanium acted as a superb regulator of the particle size and morphology, enhancing their fineness and uniformity. Inclusion of germanate ions also increased the electrophoretic mobility and hydrodynamic surface charge density of the particles by reducing their size and by inducing a more stochastic distribution of terminal ionic groups due to the bending of the crystal facets. Overall, the doping of HAp with germanate ions facilitated the production of narrowly dispersed nanorods with a moderately enhanced structural disorder and with a pronounced potential for the biomedical niche.

1. Introduction

Hydroxyapatite (HAp) is the sparsely soluble calcium phosphate phase constituting the major and the only inorganic portion of the human boney and dental tissues. Because it is being synthesized endogenously, by humans and all other mammals as well as most vertebrates, HAp presents an epitome of biocompatibility among materials in use for biomaterial applications. One corollary of this omnipresence of HAp in the living world comes in the form of its having relatively

moderate biological activities. When more active biomaterials are sought, HAp is either incorporated into composites or amended by various physical or chemical procedures.

One hallmark of HAp is its flexible crystal lattice capable of incorporating relatively highly charged calcium and phosphate ions and being traversed by the hydroxyl ion channels that connect to the hydrated diffuse ion sheath covering the surface in a rather idiosyncratic manner [1]. This combination of structural effects predisposes HAp for an exceptional tolerance to defects and, in turn, for an easily

---

accomplishable incorporation of foreign ions. These foreign ions substitute the constitutive calcium, phosphate and, occasionally, hydroxyl ions and either add the new or augment the preexisting properties in HAp. Because of the relative ease of their production, such substituted HAps have grown over the last few decades into a mainstream strategy for rendering HAp more efficacious for specific biomedical applications. For example, doping with zinc is commonly done to increase the osteogenic potential of HAp [2]; doping with selenite has added a triad of antibacterial, osteogenic and anti-carcinogenic properties to HAp [3]; doping with copper or silver has added antibacterial properties to it [4, 5]; doping with silicon aids bone regeneration when using HAp as an implant [6]; doping with vanadium has endowed HAp with photocatalytic properties [7]; doping with iodine or hafnium has rendered HAp applicable for radiographic imaging [8] or radiotherapies [9], respectively, and so on.

A study from 2020, in fact, compiled all the elements that had been used until then as dopants in HAp and concluded that 72 out of 118 elements of the Periodic Table had been incorporated inside HAp [10]. However, after excluding radioactive elements and noble gases, and considering only the elements realistically incorporable inside HAp, it turned out that ~90% of them had been used as dopants, with only 9 of them yet to be used as such, including Be, Sc, Ge, Br, Rb, Os, Ir, Hg, and Tl. Since this report was released, Rb-doped HAp was fabricated and used as a component of electrospun composite scaffolds [11]. The fact that Hg has been largely banned for use in the industrial world explains for the lack of past and, very likely, future studies on Hg-doped HAp. On the other hand, there has been a plethora of studies focused on the development of HAp for the sequestration of toxic Hg ions from the environment [12,13], meaning that Hg-substituted HAp is by no means an alien on the list of ion-substituted HAps in literature, which is not even to mention that with 116 pm in radius, Hg^{2+} ion would technically be a viable substitute for Ca^{2+} ions in HAp. The other 7 elements, however, could lead to exciting new properties in HAp, with the caveat that some of them suffer from the apparent size discrepancy issues. Beryllium, for example, is a divalent cation and it would be a good replacement for calcium had it not been for the large difference between the radii of the two cations: 45 vs. 100 pm, respectively. In addition, beryllium is a very light metal and its effects on HAp are likely to be limited to nucleation impediment and altered solubility, similarly to the effects accomplished by Li [14] or the oft-so-called "spectator" ion that Na is [15], notwithstanding the fact that Na-substituted HAp apparently has exhibits enhanced osteoconductivity as well [16]. B^-, likewise, at 182 pm in radius, is larger than the hydroxyl ion (153 pm), and unlike other halogenic anions such as F^- or Cl^-, it would have a hard time squeezing into an already tight hydroxyl channel where the rotation of the hydroxyl group is severely impeded as-is. The other five elements exist in ionic states that are not readily compatible with HAp, the most critical case of which is with Os, which forms valencies higher than or equal to +4 only. For such elements, which include also Ir, Sc, Tl and Ge, the most realistic dopants are their oxyanions. In fact, compared to the monatomic cations, which are characterized by a comparatively low atomic weight, high diffusivity and chaotropy, kosmotropic oxyanions could be argued to present a more stable substitute in HAp, capable of eliciting more predictable and consistent effects on the material properties [17].

Germanium is one of these 8 elements that had not been used as dopants in HAp yet. With the electronic configuration of $[Ar]3d^{10}4s^24p^2$, it forms stable oxidation states of +2 and +4, where the latter is both more stable and more frequent [18], forming the most common germanium oxide, GeO_2, and germanate ions including GeO_3^{2-} and GeO_4^{4-}. At the first sight, the divalent germanium ion, Ge^{2+}, which forms compounds known as germylenes, appears as an ideal dopant for HAp, where it would substitute Ca^{2+} ions, if it were not only for the proneness of Ge^{2+} for oxidation [19]. Quadrivalent germanium, Ge^{4+}, therefore, presents a more practical ionic substitute in HAp. Although Ge^{4+} could theoretically replace Ca^{2+}, there are both size and charge limitations

involved, given that Ge^{4+} is significantly smaller than Ca^{2+} (67 vs. 114 pm for crystal ionic radii) and there is also an apparent difference in the valence state between the two ions (+4 vs. +2). For this reason, the oxyanion of Ge^{4+} is likely to present the germanium dopant most readily incorporable into the HAp lattice. Ge^{4+} is larger than Si^{4+} (67 vs. 54 pm for crystal ionic radii) of the orthosilicate, SiO_4^{4-} groups, the closest common valency analog for Ge^{4+} among the oxyanionic dopants in HAp, and therefore the size of the GeO_4^{4-} ion does not seem as convenient for the replacement of the phosphate ion, its natural substitute in HAp, given the minimal difference in the size of the P^{5+} ion and that of the Si^{4+} ion: 52 vs. 54 nm. Therefore, a considerable concentration of defects is expected to form in the material due to strain effects resulting from the substitution of constitutive phosphates with germanates. Still, the successful prior incorporation of vanadate ions including V^{4+} and V^{5+} with 72 and 68 pm in crystal ionic radii, respectively, or an ion such as titanate, which contains the Ti^{4+} ion with 74.5 pm in radius has indicated that the incorporation of germanate is very much possible. Correspondingly, the goal of this study has been to produce the first germanium-substituted HAp (Ge-HAp) by doping HAp with germanate ions.

Because new forms of ion-substituted HAp are mostly being developed for biological applications, it is worth discussing briefly what biological properties the presence of Ge^{4+} might add to HAp. Neither germanium nor germanate, however, do not have any known biological roles. Even though germanium is a nontoxic element [20] noted for its antitumor, antiviral, antiaging and anti-inflammatory activities [21], its applications in biomedicine have been, to say the least, sparse. In fact, most of the uses for germanium in biotech labs have come in the form of germanium-based hemispherical lenses, such as those used in attenuated total reflection (ATR) Fourier transform infrared spectroscopy (FTIR) [22,23]. Because of its narrow band gap of only 0.67 eV at 300 K, the high refractive index of 4.0 in the mid-IR region and the high charge carrier mobility of nearly 4000 cm^2 $V^{-1}s^{-1}$ for electrons and 2000 cm^2 $V^{-1}s^{-1}$ for holes, germanium semiconductors have also found a large use as detectors in medical imaging spectroscopies utilizing high-energy ionizing radiation, such as γ-rays [24] and X-rays [25], while also being sensitive to lower-energy $α/β^-$ particulate radionuclides [26]. This combination of nontoxicity, stability and optical activity has singled out Ge as possibly the best candidate for quantum dots useable in bioimaging [27]. Ge nanoparticles have also been used successfully as drug delivery carriers [28], with their IR photoluminescence making them a potential candidate for theranostic applications combining targeted delivery and fluorescent tracking. One evidence of this potential has come in the form of a complete eradication of tumors in mice after Ge/GeO₂ nanoparticles were injected intravenously, exhibiting a synergetic photothermal and photodynamic effect triggered by the photoabsorption in the near-IR region [29]. One of the biological properties noted sparsely in the literature has been the antibacterial activity of both metallic Ge [30,31] and organogermanic compounds [32,33]. In comparison, the comparative activity of germanate ions has been vastly understudied, save the one or two sporadic reports that did demonstrate a moderate [34,35] or considerable [36] antibacterial activity of compounds involving this ion. Finally, limited evidence emerging from a recent *in vivo* study published in Ukrainian, albeit devoid of any structural data, seems to suggest that HAp supplemented with germanium may have an overwhelmingly positive effect on bone regeneration relative to pure HAp and other pure calcium phosphate phases [37].

2. Materials & methods

2.1. Synthesis

Because of the global shortage of germanate powders, sodium germanate, Na_2GeO_3, as the precursor for the synthesis of Ge-HAp was prepared by calcination of a powder mixture of NaOH and GeO_2 (Sigma Aldrich, Germany). NaOH was chosen instead of the more common

Na_2CO_3 because of the higher decomposition temperature of the latter compound. To prepare Na_2GeO_3, 1.9590 g NaOH and 2.5119 g GeO_2 were homogenized and annealed first at 720 °C and then at 810 °C, for 15 h each. To ensure that the reaction reached stoichiometric completion, the amount of NaOH used was by 2 mol.% higher than the stoichiometric. XRD analysis was performed to confirm that no secondary phases were present and that the nature of the sample was monophasic.

A previously developed procedure [38] was adapted for the synthesis of pure, Ge-free HAp and Ge-HAp. Accordingly, two alkaline solutions were prepared: a Ca^{2+} one and a PO_4^{3-} one. The Ca^{2+} solution was prepared by dissolving 2.8 g of $Ca(NO_3)_2 \times 4H_2O$ (Sigma Aldrich, Germany) in 11 ml of distillated water and then adding 1.8 ml of 25% NH_4OH to the solution, after which distilled water was added up to the total volume of 23 ml. The PO_4^{3-} solution was prepared by mixing 0.44 ml of 85% H_3PO_4 with 9.2 ml of water, then adding 1.2 ml of 25% NH_4OH, 1.53 ml of 0.5 M aqueous solution of Na_2GeO_3, and distilled water up to the total volume of 18.5 ml and 25% NH_4OH up to the total volume of 30 ml. The molar ratio of PO_4^{3-}-to-GeO_3^{2-} in the reaction solution was adjusted to 10:1 so that in the case of stoichiometric precipitation, it would yield the following formula for the unit cell of Ge-HAp: $Ca_{10-x}(PO_4)_{5.45+y}(GeO_3)_{0.55}(OH)_{2-z}$, where x, y and z denote adjustments due to charge balance reasons necessary because of the substitution of trivalent phosphates with divalent germanates. The PO_4^{3-} solution was preheated to 50 °C to dissolve the $(NH_4)_3PO_4$ crystals and then it was added dropwise into the magnetically stirred Ca^{2+} solution. The resulting 70 ml colloidal suspension was transferred to a 100 ml Teflon-lined stainless steel autoclave and the hydrothermal reaction was carried out at 150 °C for 6 h. After the reaction was over and the reactor cooled down to room temperature, the precipitate was centrifuged, washed repeatedly until pH 7 was reached and subjected to a two-step lyophilization process, first at −10 °C and 0.37 mbar for 1 h, and then at −54 °C and 0.1 mbar for 3 h. Lyophilization is essential to prevent the irreversible formation of HAp particle aggregates, which tends to take place when the liquid between the particles is removed by drying under the ambient conditions or at elevated temperatures [39]. When gel-like precipitates are dried via sublimation rather than evaporation, this aggregation is prevented and more individualized particles are obtained [40].

2.2. Characterization

Field-emission scanning electron microscopy (FE-SEM) was performed on a Carl Zeiss ULTRA Plus microscope at the electron acceleration voltage of 3 kV and the working distance of 3.9 mm. Zeta potential was measured on a NanoBrook instrument (Brookhaven) at a series of pH values in a 1 mM aqueous solution of KCl. The phase purity and the crystal structure of the as-prepared HAp and Ge-HAp powders were determined using X-ray diffraction (XRD) on a Bruker AXS D4 Endeavor device utilizing Cu–Kα radiation. Maud version 2.91 was used for the Rietveld refinement of the obtained diffractograms. Fitting was performed with the standard HAp CIF file reported in Ref. [41] with respect to the background and scale, basic phase parameters, microstructure, crystal structure, crystallinity, and strain parameters. The crystal structures containing the atomic coordinates obtained from the Rietveld refinement were plotted using CrystalMaker software version 10.7.2. Energy-dispersive X-ray spectroscopy (EDS) (Inca 400, Oxford instruments) was used for the qualitative elemental analysis. For this purpose, integrated intensities of the three major Ca peaks and of one major peak for O, P and Ge each were calculated (OriginPro 2016) and used to derive the atomic percentage of each element in the material.

FTIR measurements were performed on a Thermo Scientific™ Nicolet™ iS™10 spectrometer equipped with an ATR accessory in the 400–4000 cm^{-1} spectral range. Crystallinities were estimated from the FTIR spectra as inversely proportional to the full width at half maxima (FWHM) of the 1025 cm^{-1} $\nu3$(P–O) band and the 560 cm^{-1} $\nu4$(P–O) band deconvoluted using a multiple peak-fitting Gaussian routine

(OriginPro 2016). Backgrounds were subtracted prior to the peak integration routine using manually selected 2nd derivative anchor points (OriginPro 2016). FTIR peak asymmetry was taken as equivalent to the absolute ratio between the left and the right half peak widths. Crystallinity was estimated from the FTIR spectra by assuming its inverse correlation with respect to the FWHM of the dominant bands [42].

3. Results and discussion

One immediate effect that germanate ions exerted on HAp already during the synthesis stage could be seen by comparing the morphologies of the as-prepared particles of HAp and Ge-HAp in Fig. 1. Specifically, whereas the hydrothermally obtained HAp particles were in the form of elongated plates spanning well over a micron in length and several hundred nanometers in width, Ge-HAp particles were significantly finer, having nanoscale (<100 nm) dimensions in all three spatial directions. The tendency toward the uniaxial growth along the c-axis, which is consequential to the hexagonal crystal structure of HAp, was preserved, but also severely hindered, resulting in rod-shaped particles that had nowhere as large of the aspect ratios, let alone dimensions, as those of Ge-free HAp. Interestingly, Ge-HAp particles exhibited a markedly higher level of uniformity with respect to their morphologies and sizes than HAp particles did. On average, Ge-HAp particles had around 70 nm in length and about 15 nm in width, with the ensuing aspect ratio of 4–5. Their basal planes displayed the characteristic hexagonal features, being an indirect evidence of their growth along the crystallographic c-axis, which is normally most favorable for HAp [43,44]. The central tips topping these basal hexagons are explained by the fact that the fastest growing faces on a crystal are also those disappearing from its surface the fastest [45], in this case leaving the prominent {111} faces in lieu of the (001) one. These morphological differences combined indicate that germanate ions affected the nucleation and crystal growth remarkably and rather desirably from the perspective of controlled fine particle synthesis. To confirm the reproducibility of HAp synthesis under the hydrothermal conditions employed here, the morphological outcomes of the process were compared with those from earlier studies that utilized similar conditions and obtained highly similar results [46–48].

There are two ways of explaining mechanistically this morphological difference between Ge-HAp and HAp, one being the potential ability of germanate ions to increase the nucleation rate, which would lead to the observed greater concentration of finer particles than it was the case for Ge-free HAp, and the other one involving the hindrance of the aggregation of the fine particulates in the non-classical crystal growth pathway, which HAp has been known to obey for a very long time now [49–51]. The former effect is rather difficult to envisage as realistic and the latter one presents the most likely candidate for explaining the finer particle size of Ge-HAp as compared to that in HAp. Here, adsorption along the growing crystal faces by the foreign oxyanion and the hindered attachment of the growth units, be they ions, clusters or ultrafine nanoparticles, presents a possible mechanism explaining this growth retardation effect achieved by the germanate impurity. In addition to this external effect by which germanate ions may obstruct the non-classical growth pathway, they may exert a similarly disruptive effect from the inside out as well. Correspondingly, by getting incorporated inside the nascent lattice of the growing nuclei, germanate ions may impede the kinetics of coalescence of the growth units, which is known to depend on the stochastic search for an optimal orientation [52]. The increase in hydrophobicity and the corresponding decrease in the hydration energy resulting from the addition of germanate ions, which are more similar to silicates than to phosphates from this standpoint, may be an important contributor to this growth impediment, too. The addition of germanate is also expected to increase the surface-solution interfacial free energy, which is directly proportional to the degree of supersaturation required to overcome this energy barrier and induce the growth [53], providing for the fundamental thermodynamic obstacle standing in the way of the unobstructed growth.
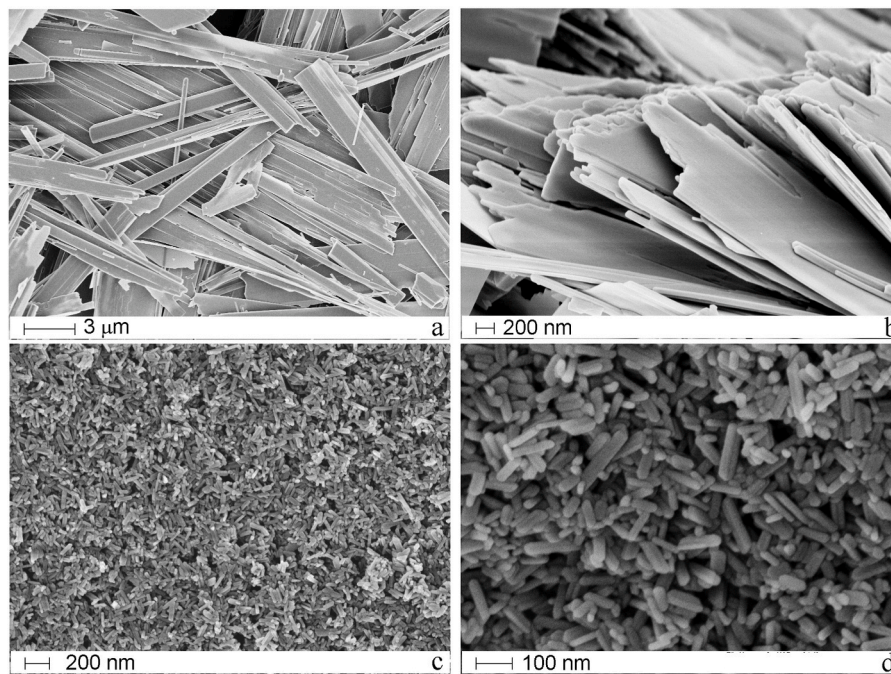
Fig. 1. SEM images of HAp (a–b) and Ge-HAp (c–d). Scale bars are 3 μm (a), 200 nm (b, c), and 100 nm (d).

Further, the EDS analysis confirmed the presence of Ge as the fourth most abundant detectable element in Ge-HAp, right after Ca, P and O (Fig. 2). Based on the results of the quantitative analysis of the dispersive spectra shown in Table 1, the amount of germanium in Ge-HAp was equal to 0.876 at.%. This corresponds to the tentative HAp stoichiometry of $Ca_{10-x}(PO_4)_{5.62+y}(GeO_3)_{0.38}(OH)_{2-z}$, according to which approximately 1 in 14 phosphate groups got replaced with germanate, which is just slightly lower than the intended 1 in 10. Comparison with the intended stoichiometry used in the preparation protocol, namely $Ca_{10-x}(PO_4)_{5.45+y}(GeO_3)_{0.55}(OH)_{2-z}$, shows that approximately two-thirds of the germanate ions introduced into the hydrothermal solution got incorporated into HAp, whereas one-thirds remained in the supernatant. These elemental characterization results provide a definite testament to the successful incorporation of germanate ions into the lattice of HAp.

Surface charge characterization showed an increase in the absolute value of zeta potential, from −9.5 mV for pure HAp at pH 7.0 to −12.2 mV for Ge-HAp at the same pH (Table 1). This increase in the density of

Table 1

Elemental composition of HAp and Ge-HAp, as obtained from the quantitative analysis of energy dispersive spectra, along with the zeta potential, ζ, and electrophoretic mobility, μ_e, at pH 7.0 for HAp and Ge-HAp.

Sample	Ca (at. %)	P (at. %)	O (at. %)	Ge (at. %)	ζ (mV)	μ_e (μmcm/ Vs)
HAp	50.82	33.17	16.01	0.00	- 9.50	- 0.81
Ge-HAp	47.27	34.63	17.23	0.88	- 12.23	- 0.96

negative charges on the particle surface and in the hydrodynamic sphere surrounding the particle surface can be a secondary effect of the redistribution of terminal groups induced by the inclusion of germanate ions. In a simplest scenario, this terminal group redistribution may be caused by changes to the particle morphology. Namely, more oval particles tend to exhibit a more stochastic distribution of terminal ionic groups than the faceted particles do. Therefore, it is conceivable that the rounding of
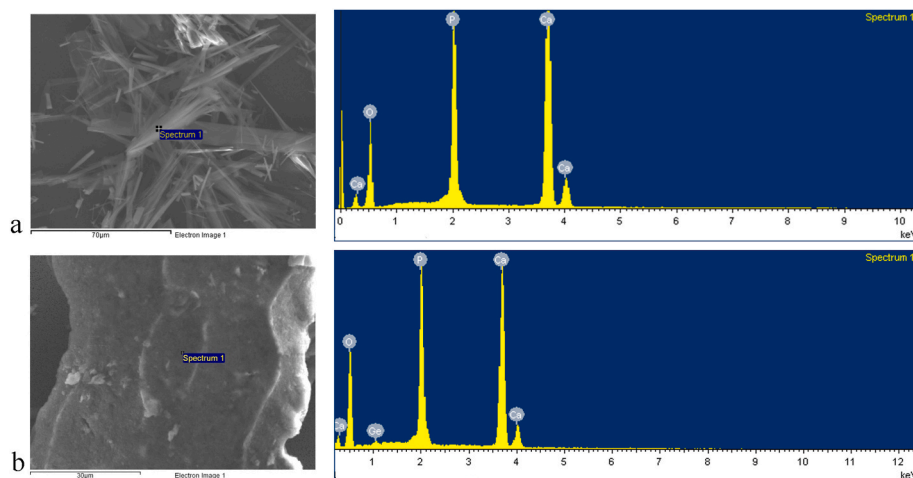

Fig. 2. Energy dispersive spectra with the elemental characterization of HAp (a) and Ge-HAp (b), denoting the three elements detected in HAp, namely Ca, O and P, and the four elements detected in Ge-HAp, namely Ca, O, Ge, and P.

the particles consequential to the addition of germanate ions to HAp may have promoted a less selective termination of the facets by Ca^{2+} ions and made the negatively charged groups, including PO_4^{3-}, HPO_4^{2-}, GeO_3^{2-} and OH^-, more prominent on the surface. At the same time, the electrophoretic mobility of anisotropic particles is more prone to error during measurements because of the spherical geometry approximation used by default during the dynamic light scattering analyses. Last but not least, the significant reduction in the particle size caused by the incorporation of germanate ions into the lattice of HAp may have also contributed to this increase in the absolute value of zeta potential. Even when the particle size and shape do not affect the surface charge density due to aforementioned reasons, their effect on the electrophoretic mobility, from which zeta potential is calculated, is omnipresent, simply because particles with the same surface charge but of different size and shape will move with different velocities in the electric field [54]. This effect is clearly evidenced by the higher mobility of Ge-HAp nanoparticles than that of HAp (Table 1). At the same time, however, smaller particles are more affected by the fluid flow and by the Brownian motion of neighboring particles, whereas the larger particles are more prone to aggregation and gravity affects. All these factors combined result in the generally higher absolute zeta potential values for the smaller particles as compared to their larger counterparts with an identical chemical composition [55].

Regarding the mechanism of inclusion of germanate ions into the lattice of HAp, it involves the competition with phosphates for the sites normally occupied by the latter ions in pure stoichiometric HAp. As shown in Fig. 3, the only viable sites for germanates to occupy in the lattice of HAp are those taken on by phosphates, given that germanate ions are too large to replace the hydroxyl anion. Even carbonate as an oxyanion considerably smaller than germanate can enter the hydroxyl channel only under a high-temperature treatment or under specific biomineralization conditions of growth [56].

XRD analysis of HAp and Ge-HAp revealed a rather low level of distinction between the diffractograms to the naked eye save for the slightly higher background noise present in the XRD pattern of Ge-HAp as compared to that of HAp (Fig. 4). All of the major HAp reflections were detected in both samples, without any secondary calcium
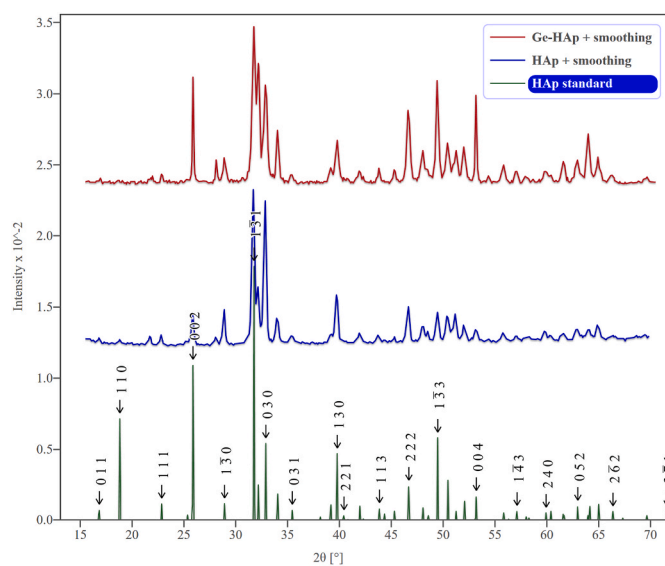

Fig. 4. XRD patterns of HAp and Ge-HAp in comparison with the HAp standard.

phosphate or germanium phases in them. Alongside proving the phase compositional purity of both HAp and Ge-HAp, XRD patterns were used to derive the crystal structure and strain parameters for the two materials through Rietveld refinement. The results shown in Table 2 demonstrate an evident, statistically significant increase in both lattice constants, *a* and *c*, after the integration of germanate ions into the crystal structure of HAp. Correspondingly, the lattice expanded in the direction parallel to the basal plane by 0.00185 Å and along the screw plane axis by 0.00647 Å. Simultaneously, the average crystallite size decreased by little over 4 nm and the microstrain tripled. This lattice expansion can only partially be due to the size effects, namely the replacement of smaller phosphates with larger germanates, given that the radius of the germanate ion, GeO_3^{2-}, equaling 242 pm, is only slightly larger than the ionic radius of the PO_4^{3-} ion (238 pm). The biggest contribution to the detected lattice expansion and disordering, albeit minor in degree, must have come from the different mechanisms that compensated for the charge imbalance caused by the substitution of the trivalent phosphates with the divalent germanates. These mechanisms include the formation of paired hydroxyl and calcium vacancies, the retention of a proton by the phosphate group, and others. However, common to all of these atomic-scale mechanisms is the formation of defects and lattice straining, explaining the expansion of the lattice, the reduction of crystallinity and an increase in the microstrain consequential to the doping of HAp with germanate.

The difference in the crystal structure of purely HAp domains in HAp and Ge-HAp is evident from Fig. 5. As it can be further seen from Table 3, the most dramatic difference in atomic coordinates was observed for the O1-3 phosphate oxygens, especially along the y axis, and for the O4 hydroxyl oxygen, which is confined to the channel that forms the edges
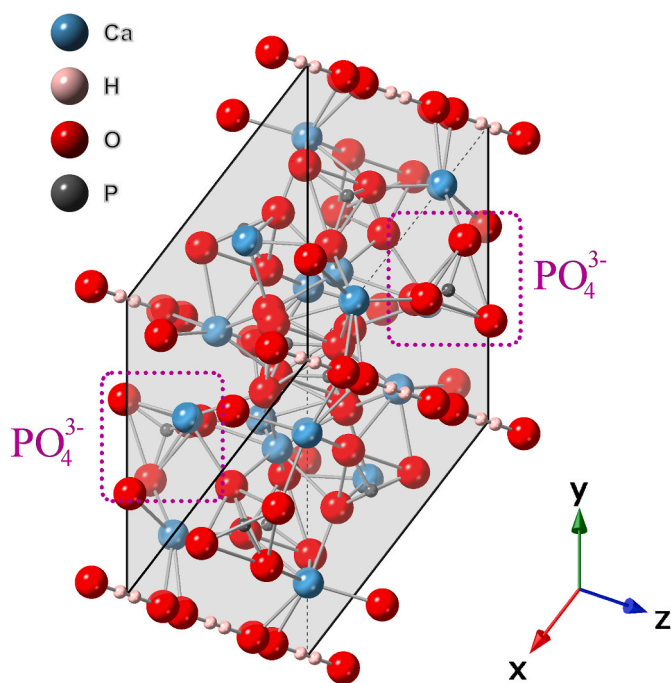

Fig. 3. Crystal structure of HAp viewed down the [111] axis, denoting two of the phosphate groups as the only viable sites for the accommodation of germanate. The unit cell of HAp is demarcated in gray.

Table 2

Lattice parameters, crystallinity and microstrain obtained from the Rietveld refinement of the diffractograms of HAp and Ge-HAp in comparison with the HAp standard.

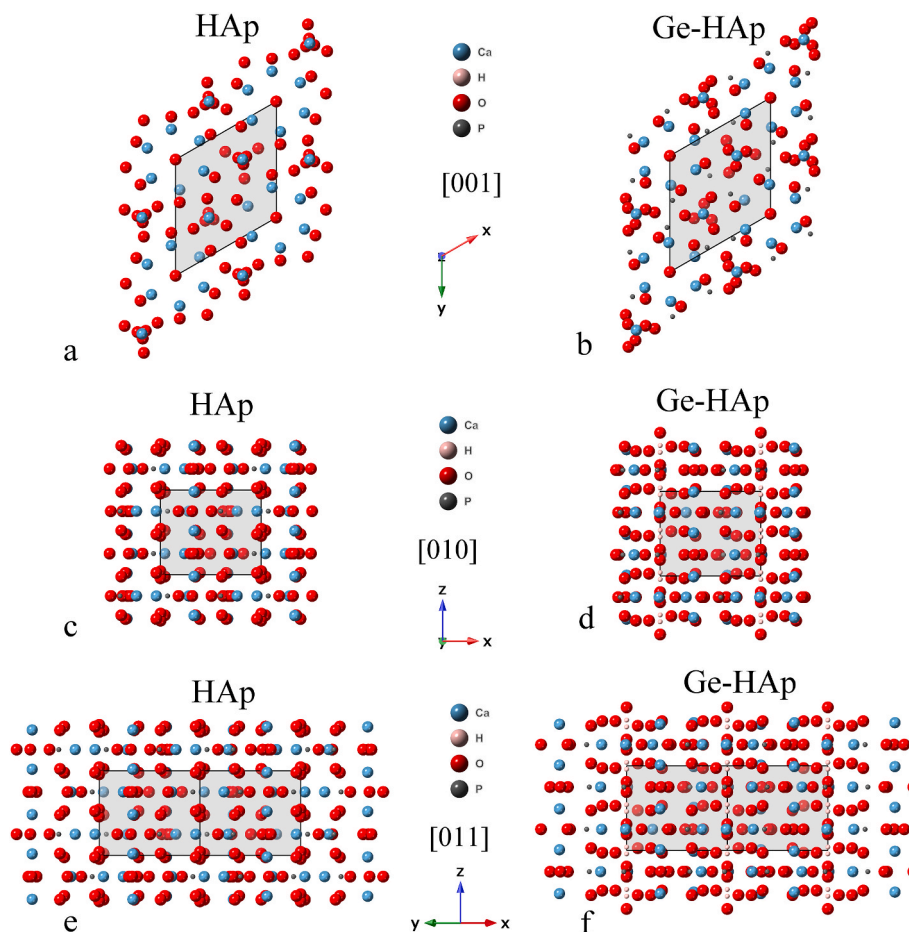| Powder	a (Å)	c (Å)	Crystallinity (nm)	Microstrain (%%)
Standard HAp	9.42100	6.88000	100	0
HAp	9.44631 ± 0.00366	6.88978 ± 0.00271	52.94 ± 1.36	1.45 ± 2.30
Ge-HAp	9.44816 ± 0.00152	6.89625 ± 0.00137	48.78 ± 1.84	4.40 ± 3.30

Fig. 5. Crystal structures of HAp (a, c, e) and Ge-HAp (b, d, f) plotted using the atomic coordinates obtained from the Rietveld refinement. Projections are down the c, [001] axis (a–b), b, [010] axis (c–d), and [011] axis (e–f). The unit cell of HAp is demarcated in gray.

Table 3
Atomic coordinates x, y, and z for the constitutive Ca, P and O atoms in HAp lattice for the HAp standard, for HAp, and for Ge-HAp. Italicized coordinates were fixed during the calculation, whereas all the other ones were refined. Unit cell angles were kept constant at $\alpha = 90^\circ$, $\beta = 90^\circ$, and $\gamma = 120^\circ$.

Atom	Wyckoff position	HAp standard			HAp			Ge-HAp		
		x	y	z	x	y	z	x	y	z
Ca1	4f	0.333	0.667	0.000	*0.333*	*0.667*	−0.018	*0.333*	*0.667*	−0.009
Ca2	6h	0.245	0.993	0.250	0.239	0.958	*0.250*	0.248	0.990	*0.25*
P	6h	0.398	0.370	0.250	0.402	0.332	*0.250*	0.397	0.370	*0.25*
O1	6h	0.327	0.485	0.250	0.296	0.674	*0.250*	0.342	0.5825	*0.25*
O2	6h	0.586	0.465	0.250	0.685	0.506	*0.250*	0.588	0.438	*0.25*
O3	12i	0.341	0.256	0.073	0.390	0.348	0.022	0.352	0.241	0.027
O4/OH	4e	0	0	0.188	*0*	*0*	−0.042	*0*	*0*	0.190

of the tetragonal unit cell projection down the *c*-axis. The most drastic change in the positioning of this oxygen occurred, naturally, along the z direction. Obviously, these shifts are corollaries of the incorporation of germanate ions at the sites otherwise reserved for phosphate groups, with the effect extending to the anions locked inside the hydroxyl channel. This substitution promotes the rearrangement of the lattice, which is most critical in the direct vicinity of the dopant oxyanion. However, as it is being evidenced here, the replacement of phosphate tetrahedra with pyramidal germanate ions is such that it necessitates the rotation of the adjacent phosphate groups, with effects extending across numerous unit cells, affecting the long-range symmetry. This adds to the effects of defect formation arising to compensate the charge imbalance caused by the replacement of trivalent phosphates with divalent germanates.

FTIR analysis overwhelmingly corroborated the findings of the

crystallographic analysis. In the wavenumber region of a lower interest (Fig. 6a), 1500–4000 cm^{-1}, the scissoring bend of the water molecules (1550 cm^{-1}) was detected along with the traces of adsorbed water (3800–2600 cm^{-1}) and the symmetric stretch of the channel hydroxyl ions (3608 cm^{-1}). In the wavenumber of region of a higher interest (Fig. 6b), 400–1500 cm^{-1}, as with the XRD analysis, the spectral differences appeared negligible to the naked eye, but a closer inspection of the spectra revealed a definite difference between them. First, as shown in Fig. 7a-b, the two most intense stretching bands in the spectra of both materials, namely the triply degenerated antisymmetric stretching mode vibration of the P–O bond, $\nu3$, peaking at 1028 cm^{-1}, and the fully symmetric non-degenerated stretching mode of the P–O bond, peaking at 962 cm^{-1}, experienced evident upshifts upon the incorporation of germanate ions into the HAp lattice. Clearly, the expansion of the lattice reduces the environmental influence of adjacent ions on the active
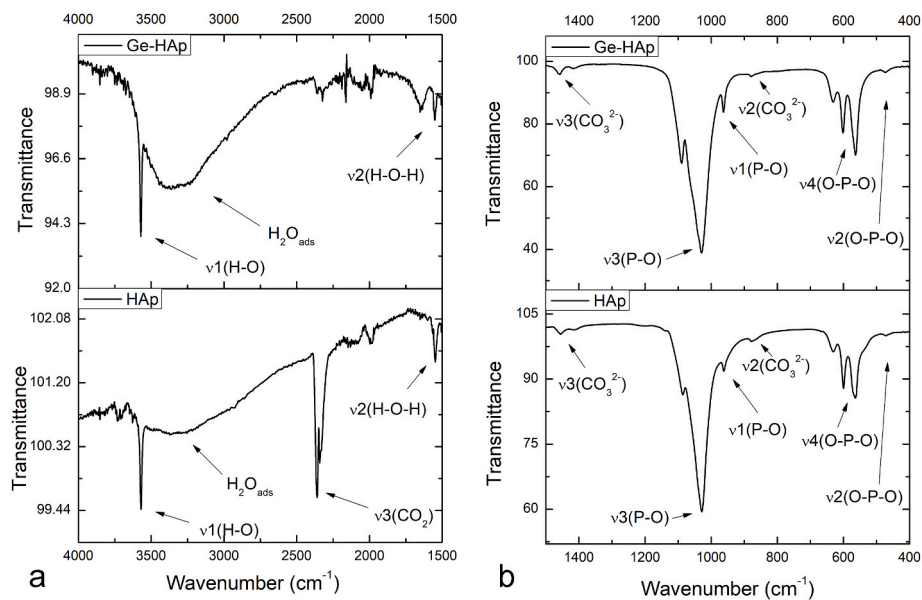
Fig. 6. FTIR spectra of HAp and Ge-HAp in the 4000–1500 cm^{-1} (a) and 1500–400 cm^{-1} (b) wavenumber ranges.
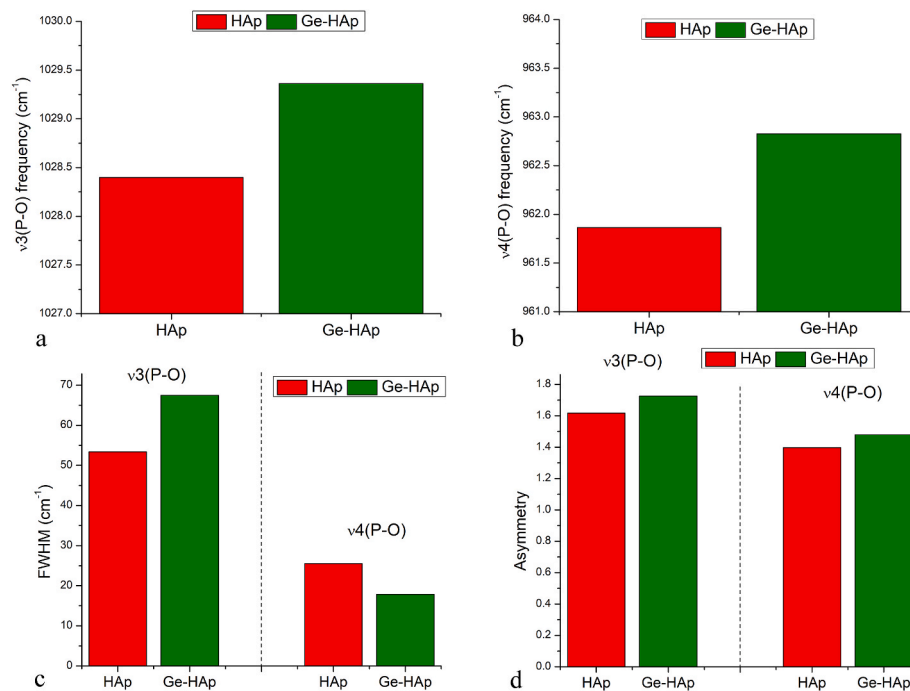

Fig. 7. Peak frequencies of the two dominant vibration modes in the FTIR spectra of HAp and Ge-HAp: the antisymmetric $\nu3$ stretch (a) and the antisymmetric $\nu4$ bend (b). The difference in the FWHM (c) and the asymmetry (d) of these two vibration modes for HAp and Ge-HAp.

modes, which increases the frequency of stretching vibrations, bringing them closer to the wavenumbers that these modes would possess in an isolated state. For this reason, the frequency of both P–O stretches increased with the introduction of germanates into the HAp lattice.

Secondly, the reduction of crystallinity is usually reflected in the broadening of the FWHM of FTIR bands [57]. This effect is the consequence of the increased heterogeneity of environments surrounding the active vibration groups when the crystalline order is diminished. This increased heterogeneity of states becomes naturally reflected in the broadening of the spectral lines. This effect is shown in Fig. 7c, where the increase in the FWHM of the most intense band in the spectrum of Ge-HAp, namely the $\nu3$ band, is shown relative to their FWHM values in

the spectrum of HAp. One caveat here is that this vibration state dispersion effect did not apply to the second most intense band in the spectrum, namely the triply degenerated bending mode, $\nu4$, of the O–P–O bond, notwithstanding that bending modes are oftentimes exceptions to this and the aforementioned trend that usually apply best to the stretching modes. Moreover, the increased structural disorder is frequently reflected in the increased asymmetry of the vibrational bands, and so was the case here. As shown in Fig. 7d, the degree of asymmetry of both the $\nu3$ and the $\nu4$ bands increased with the introduction of germanate ions into HAp, attesting to the partial loss of the structural order entailing this doping process.

Finally, the effects of the germanate dopant on carbonates naturally

present as phosphate substitutes in any HAp synthesized under ambient conditions were analyzed using FTIR. Fig. 8a shows the FTIR regions occupied by the most intense carbonate band, namely the antisymmetric, $\nu3$ stretch whose central component peaked at 1455 cm^{-1}. The component of this stretch appearing at a lower energy corresponds to the B-type carbonate in HAp, which occupies phosphate group sites, whereas the component found at a higher energy corresponds to the A-type carbonate in HAp, which gets accommodated inside the hydroxyl channel [58]. Typically, whereas the B-type carbonation occurs under any conditions, including most prominently the ambient, the A-type carbonation normally requires elevated temperatures for this less entropic accommodation to be initiated [56]. The central component of the $\nu3$ stretch is usually associated with the mixed AB type [58] and its dominance over the A-type and the B-type components suggests the predominantly mixed nature of carbonation in both HAp and Ge-HAp. This effect owes mostly to the relatively energetic, hydrothermal conditions of synthesis employed here. However, as it is seen from Fig. 8b, the ratio of the B-type to the A-type carbonates in HAp visibly drops with the addition of germanate, which is expected in view of the aforementioned inclusion of germanate ions in place of phosphates. Simply, this integration of germanate ions in place of phosphates leaves less room for the accommodation of adventitious carbonates on these lattice sites, as the result of which the ratio of the B-type to the A-type carbonates decreases. At the same time, however, as also shown in Fig. 8b, with the addition of germanate ions to HAp, the total amount of carbonates estimated from the percentage that the $\nu3$ carbonate band occupies relative to the rest of the spectrum increases by more than three times. This is a natural corollary of the reduction of crystallinity of HAp entailing the introduction of germanates. Because both germanate and carbonate ions reduce the crystalline order upon their inclusion in the structure of HAp, it is expected based on La Châtelier's principle that the reduction of this order caused by the inclusion of the former species would increase the capacity for the accommodation of the latter species.

4. Conclusions

The first synthesis and characterization of HAp doped with germanium ions is being reported. To promote the stability of the ionic substitution, germanium was deliberately integrated into the HAp lattice in the form of germanate, GeO_3^{2-}, ions, which took the place of constitutive phosphates, thereby altering the crystallographic order of the lattice. Approximately two thirds of the germanate ions introduced into the hydrothermal solution got incorporated into the HAp lattice, yielding the approximate stoichiometry of $Ca_{10-x}(PO_4)_{5.62+y}(GeO_3)_{0.38}(OH)_{2-z}$. Germanate proved to be an excellent regulator of the particle size and shape, as its addition promoted the conversion of irregular abutting microsized plates into uniform rod-shaped nanoparticles with sizes well under 100 nm across all the dimensions. By replacing tetrahedral phosphate groups in the crystal structure of HAp, trigonal germanate isotropically expanded the HAp lattice, increased the microstrain and reduced the crystallinity. This disordering effect was attributed partly to the larger size of the germanate ion than that of the phosphate ion and partly to the defects and bond distortions invoked to compensate for the charge imbalance brought about by the replacement of the trivalent phosphates with the divalent germanates. Vibrational spectroscopic analyses corroborated these crystallographic effects by demonstrating the enhanced heterogeneity of the stereochemical environment surrounding the active modes after germanate ions were incorporated into the lattice of HAp through consistent frequency upshifts, broadening of the bands and increases in the peak asymmetry. Conforming to La Châtelier's principle, this reduction of the crystallographic order increased the capacity of the material for integration of adventitious carbonates. However, the inclusion of germanate ions induced a partial shift of these carbonates to the hydroxyl channel sites. Inclusion of germanate ions also increased the electrophoretic mobility and hydrodynamic surface charge density of the particles by reducing their size and by inducing a more stochastic distribution of terminal ionic groups due to the bending of the crystal facets. Overall, as it is being shown here, the doping of HAp with germanate ions facilitates the production of nanorods with a narrow dispersion of particle sizes and shapes and with moderately enhanced structural disorder. The findings reported here warrant a series of follow-up studies on assessing the biological effects of supplementing HAp with germanate ions. These future biological studies are planned to include cytotoxicity assays, antibacterial tests and other biological marker analyses.

Contributions

As per CRediT taxonomy, V.U. – conceptualization, methodology, formal analysis, visualization, writing; N.I – methodology, investigation, resources; S.Š. – investigation, resources; D.U. – supervision.

Declaration of competing interest

The authors declare that they have no known competing financial interests or personal relationships that could have appeared to influence
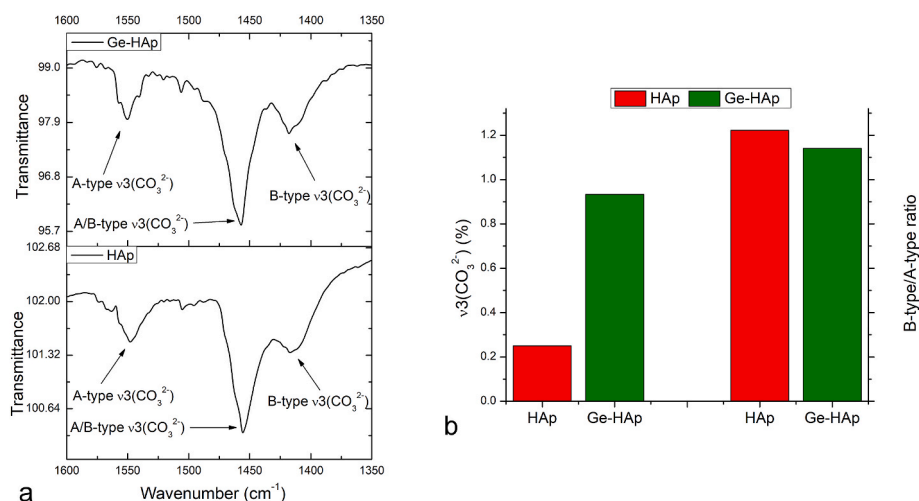

Fig. 8. FTIR spectra of HAp and Ge-HAp in the 1600–1350 cm^{-1} range, focusing on the antisymmetric $\nu3$ stretch of the carbonate anion (a). The comparison of the calculated total percentage that the $\nu3$ carbonate band occupies relative to the entire spectra of HAp and Ge-HAp (b, left Y-axis). The ratio of the B-type carbonate to the A-type carbonate in HAp and Ge-HAp (b, right Y-axis).

the work reported in this paper.

References

[1] V. Uskoković, The role of hydroxyl channel in defining selected physicochemical peculiarities exhibited by hydroxyapatite, RSC Adv. 5 (2015) 36614–36633.

[2] M. Okada, M. Oshita, M. Kataoka, Y. Azuma, T. Furuzono, Shareability of antibacterial and osteoblastic-proliferation activities of zinc-doped hydroxyapatite nanoparticles in vitro, J. Biomed. Mater. Res. B Appl. Biomater. 110 (4) (2022) 799–805.

[3] V. Uskoković, M.A. Iyer, V.M. Wu, One ion to rule them all: combined antibacterial, osteoinductive and anticancer properties of selenite-incorporated hydroxyapatite, J. Mater. Chem. B 2017 (5) (2017) 1430–1445.

[4] A. Jacobs, G. Renaudin, N. Charbonnel, J.M. Nedelec, C. Forestier, S. Descamps, Copper-doped biphasic calcium phosphate powders: dopant release, cytotoxicity and antibacterial properties, Materials 14 (9) (2021) 2393.

[5] M. Riaz, R. Zia, A. Ijaz, T. Hussain, M. Mohsin, A. Malik, Synthesis of monophasic Ag doped hydroxyapatite and evaluation of antibacterial activity, Mater Sci Eng C Mater Biol Appl 90 (2018) 308–313.

[6] T. Sun, M. Wang, Y. Shao, L. Wang, Y. Zhu, The effect and osteoblast signaling response of trace silicon doping hydroxyapatite, Biol. Trace Elem. Res. 181 (1) (2018) 82–94.

[7] M. Nishikawa, L.H. Tan, Y. Nakabayashi, T. Hasegawa, W. Shiroishi, S. Kawahara, N. Saito, A. Nosaka, Y. Nosaka, Visible light responsive vanadium-substituted hydroxyapatite photocatalysts, J. Photochem. Photobiol., A: Chem 311 (2015) 30–34.

[8] N. Ignjatović, S. Vranješ-Djurić, Ž. Mitić, D. Janković, D. Uskoković, Investigating an organ-targeting platform based on hydroxyapatite nanoparticles using a novel in situ method of radioactive 125Iodine labeling, Mater. Sci. Eng. C 43 (2014) 439–446.

[9] M.H. Chen, N. Hanagata, T. Ikoma, J.Y. Huang, K.Y. Li, C.P. Lin, F.H. Lin, Hafnium-doped hydroxyapatite nanoparticles with ionizing radiation for lung cancer treatment, Acta Biomater. 37 (2016) 165–173.

[10] V. Uskoković, Ion-doped hydroxyapatite: an impasse or the road to follow? Ceram. Int. 46 (8/B) (2020) 11443–11465.

[11] R. Al-Wafi, M.K. Ahmed, S.F. Mansour, S.I. El-dek, V. Uskoković, Physical and biological changes associated with the doping of carbonated hydroxyapatite/polycaprolactone core-shell nanofibers dually, with rubidium and selenite, J. Mater. Res. Technol. 9 (3) (2020) 3710–3723.

[12] M. Álvarez Velásquez, V. Cortes, L. Guarín Alfaro, A. Jaramillo, Y. Panqueva, A. Burgos, Synthesis and characterization of hydroxyapatite for mercury removal in polluted waters, MRS Advances 4 (2019) 3569–3577.

[13] M. Bahrami, M.J. Amiri, F. Dehkhodaie, Effect of different thermal activation on hydroxyapatite to eliminate mercury from aqueous solutions in continuous adsorption system, Int. J. Environ. Anal. Chem. 101 (2021) 2150–2170.

[14] V.V. Smirnov, S.M. Barinov, S.V. Smirnov, A.I. Krylov, O.S. Antonova, M. A. Goldberg, T.O. Obolkina, A.A. Konovalov, A.V. Leonov, Structure and thermal stability of lithium-substituted hydroxyapatite ceramics, Inorg. Mater. 55 (2019) 715–723.

[15] H. M Rootare, V.R. Deitz, F.G. Carpenter, Solubility product phenomena in hydroxyapatite-water systems, J. Colloid Sci. 17 (1962) 179–206.

[16] J. Sang Cho, S.H. Um, D. Su Yoo, Y.C. Chung, S. Hye Chung, J.C. Lee, S.H. Rhee, Enhanced osteoconductivity of sodium-substituted hydroxyapatite by system instability, J. Biomed. Mater. Res. B Appl. Biomater. 102 (5) (2014) 1046–1062.

[17] V.M. Wu, M.K. Ahmed, M.S. Mostafa, V. Uskoković, Empirical and theoretical insights into the structural effects of selenite doping in hydroxyapatite and the ensuing inhibition of osteoclasts, Mater. Sci. Eng. C 117 (2020), 111257.

[18] C. Frondel, J. Ito, Geochemistry of germanium in the oxidized zone of the tsumeb mine, south-west africa, Am. Mineral. 42 (1957) 743–753.

[19] Anon, "Germanium", Encyclop. Britannica (2022) retrieved from, https://www.britannica.com/science/germanium.

[20] Anon, Periodic Table: Germanium", Royal Society of Chemistry, 2022 retrieved from, https://www.rsc.org/periodic-table/element/32/germanium.

[21] J.M. Cho, J. Chae, S.R. Jeong, M.J. Moon, D.Y. Shin, J.H. Lee, Immune activation of Bio-Germanium in a randomized, double-blind, placebo-controlled clinical trial with 130 human subjects: therapeutic opportunities from new insights, PLoS One 15 (10) (2020), e0240358.

[22] O. Fedotova, D. Myalenko, N. Pryanichnikova, E. Yurova, E. Agarkova, Microscopic and structural studies of an antimicrobial polymer film modified with a natural filler based on triterpenoids, Polymers 14 (6) (2022) 1097.

[23] J. Meneghel, S. Passot, F. Jamme, S. Lefrançois, P. Lieben, P. Dumas, F. Fonseca, FTIR micro-spectroscopy using synchrotron-based and thermal source-based radiation for probing live bacteria, Anal. Bioanal. Chem. 412 (26) (2020) 7049–7061.

[24] D. Stanga, D. Gurau, L. Done, A. Luca, A novel virtual point detector model for high purity germanium detectors, Appl. Radiat. Isot. 181 (2022), 110107.

[25] M. Krmar, S. Shukla, K. Ganezer, Bone densitometry using x-ray spectra, Phys. Med. Biol. 55 (20) (2010) 6105–6123.

[26] O. Aviv, L. Epstein, Y. Fried, H.B. Spitz, S. Shonkor, D. Epstein, A. Naim, Z. Yungrais, H. Datz, A method to identify and localize a single hot method to identify and localize a single hot particle in the lungs using an array of high-purity germanium detectors for improved estimate of the deposited activity, Radiat. Protect. Dosim. 198 (1–2) (2022) 62–73.

[27] B. Pescara, K.A. Mazzio, Morphological and surface-state challenges in Ge nanoparticle applications, Langmuir 36 (40) (2020) 11685–11701.

[28] Y.J. Guo, F. Yang, L. Zhang, J. Pi, J.Y. Cai, P.H. Yang, Facile synthesis of multifunctional germanium nanoparticles as a carrier of quercetin to achieve enhanced biological activity, Chem. Asian J. 9 (8) (2014) 2272–2280.

[29] Y. Gao, S. Wang, C. Yang, N. An, Z. Liu, M. Yan, C. Guo, A near-infrared responsive germanium complex of Ge/GeO2 for targeted tumor phototherapy, J. Mater. Chem. B 7 (33) (2019) 5056–5064.

[30] Arslan ME, Kurt MŞ, Aslan N, Kadi A, Öner S, Çobanoğlu Ş, Yazici A. Structural, biocompatibility, and antibacterial properties of Ge-DLC nanocomposite for biomedical applications. J. Biomed. Mater. Res. B Appl. Biomater.. doi: 10.1002/jbm.b.35027. Epub ahead of print (2022).

[31] M.Ş. Kurt, M.E. Arslan, A. Yazici, İ. Mudu, E. Arslan, Tribological, biocompatibility, and antibiofilm properties of tungsten-germanium coating using magnetron sputtering, J. Mater. Sci. Mater. Med. 32 (1) (2021) 6.

[32] S. Baidya, Y. Nishimoto, S. Sato, Y. Shimada, N. Sakurai, H. Nonaka, K. Noguchi, M. Kido, S. Tadano, K. Ishikawa, K. Li, A. Okubo, T. Yamada, Y. Orba, M. Sasaki, H. Sawa, H. Miyamoto, A. Takada, T. Nakamura, A. Takaoka, Dual effect of organogermanium compound THGP on RIG-I-mediated viral sensing and viral replication during influenza a virus infection, Viruses 13 (9) (2021) 1674.

[33] E. Tanuhadi, N.I. Gumerova, A. Prado-Roller, M. Galanski, H. Čipčić-Paljetak, D. Verbanac, A. Rompel, Aluminum-substituted keggin germanotungstate [HAl (H2O)GeW11O39]4-: synthesis, characterization, and antibacterial activity, Inorg. Chem. 60 (1) (2021) 28–31.

[34] A. Avellan, M. Auffan, A. Masion, C. Levard, M. Bertrand, J. Rose, C. Santaella, W. Achouak, Remote biodegradation of Ge-imogolite nanotubes controlled by the iron homeostasis of Pseudomonas brassicacearum, Environ. Sci. Technol. 50 (14) (2016) 7791–7798.

[35] E.V. Gudzenko, N.V. Borzova, L.D. Varbanets, V.A. Ivanitsa, I.I. Seifullina, E. E. Martsinko, O.V. Pirozhok, E.A. Chebanenko, Glycosidase activity of bacteria the genus bacillus, isolated from the black sea, Mikrobiol. Zh. 81 (3) (2019) 14–26.

[36] Z. Li, J. Wang, R. Shen, N. Chen, X. Qin, W. Wang, Q. Yuan, Topological radiated dendrites featuring persistent bactericidal activity for daily personal protection, Small 17 (24) (2021), e2100562.

[37] T.P. Todosiuk, M.V. Rublenko, V.M. Vlasenko, Dynamics of hematological parameters in rabbits for osteosubstitution by hydroxyapatite ceramics doped with germanium and in complex with blood coagulation activator, Scient. Messen. Lviv Natl. Univ. Veterin. Med. Biotechnol. Series: Veterin. Sci. 23 (102) (2021) 78–86.

[38] N.L. Ignjatović, L. Mančić, M. Vuković, Z. Stojanović, M.G. Nikolić, S. Škapin, S. Jovanović, L. Veselinović, V. Uskoković, S. Lazić, S. Marković, M. Lazarević, D. P. Uskoković, Rare-earth (Gd3+, Yb3+/Tm3+, Eu3+) Co-doped hydroxyapatite as magnetic, up-conversion and down-conversion materials for multimodal imaging, Sci. Rep. 9 (2019), 16305.

[39] N.L. Ignjatović, M. Plavšić, M.S. Miljković, L.M. Živković, D.P. Uskoković, Microstructural characteristics of calcium hydroxyapatite/poly-L-lactide based composites, J. Microsc. 196 (Pt 2) (1999) 243–248.

[40] E. Trenkenschuh, W. Friess, Freeze-drying of nanoparticles: how to overcome colloidal instability by formulation and process optimization, Eur. J. Pharm. Biopharm. 165 (2021) 345–360.

[41] L. Veselinović, L. Karanović, Z. Stojanović, I. Bračko, S. Marković, N. Ignjatović, D. Uskoković, Crystal structure of cobalt-substituted calcium hydroxyapatite nanopowders prepared by hydrothermal processing, J. Appl. Crystallogr. 43 (2) (2010) 320–327.

[42] E. Amenta, H.E. King, H. Petermann, V. Uskoković, S.M. Tommasini, C.M. Macica, Vibrational spectroscopic analysis of hydroxyapatite in HYP mice and individuals with XLH, Therap. Adv. Chron. Dise. 9 (2018) 268–281.

[43] V. Uskoković, M.-K. Kim, W. Li, S. Habelitz, Enzymatic processing of amelogenin during continuous crystallization of apatite, J. Mater. Res. 32 (2008) 3184–3195.

[44] V. Uskoković, W. Li, S. Habelitz, Amelogenin as a promoter of nucleation and crystal growth of apatite, J. Cryst. Growth 316 (2011) 106–117.

[45] V. Uskoković, Chemical reactions as petite rendezvous: the use of metaphor in materials science education, J. Mater. Educ. 36 (1–2) (2014) 25–50.

[46] N. Ignjatović, Z. Ajduković, V. Savić, S. Najman, D. Mihailović, P. Vasiljević, Z. Stojanović, V. Uskoković, D. Uskoković, Nanoparticles of cobalt-substituted hydroxyapatite in regeneration of mandibular osteoporotic bones, J. Mater. Sci. Mater. Med. 24 (2) (2013) 343–354.

[47] Z. Stojanović, L. Veselinović, S. Marković, N. Ignjatović, D. Uskoković, Hydrothermal synthesis of nanosized pure and cobalt-exchanged hydroxyapatite, Mater. Manuf. Process. 24 (10–11) (2009) 1096–1103.

[48] Z.S. Stojanović, N. Ignjatović, V. Wu, V. Žunič, L. Veselinović, S. Škapin, M. Miljković, V. Uskoković, D. Uskoković, Hydrothermally processed 1D hydroxyapatite: mechanism of formation and biocompatibility studies, Mater. Sci. Eng. C 68 (2016) 746–757.

[49] K. Onuma, A. Ito, Cluster growth model for hydroxyapatite, Chem. Mater. 10 (11) (1998) 3346–3351.

[50] M. Li, L. Wang, W. Zhang, C.V. Putnis, A. Putnis, Direct observation of spiral growth, particle attachment, and morphology evolution of hydroxyapatite, Cryst. Growth Des. 16 (8) (2016) 4509–4518.

[51] V. Uskoković, Disordering the disorder as the route to a higher order: incoherent crystallization of calcium phosphate through amorphous precursors, Cryst. Growth Des. 19 (8) (2019) 4340–4357.

[52] V.K. Ivanov, P.P. Fedorov, A. Ye Baranchikov, V.V. Osiko, Oriented attachment of particles: 100 years of investigations of non-classical crystal growth, Russ. Chem. Rev. 83 (2014) 1204.

[53] O. Borkiewicz, J. Rakovan, C.L. Cahill, Time-resolved in situ studies of apatite formation in aqueous solutions, Am. Mineral. 95 (2010) 1224–1236.

[54] V. Uskoković, Dynamic light scattering and microelectrophoresis: main prospects and limitations, J. Dispersion Sci. Technol. 33 (12) (2012) 1762–1786.

[55] Y. Nakatuka, H. Yoshida, K. Fukui, M. Matuzawa, The effect of particle size distribution on effective zeta-potential by use of the sedimentation method, Adv. Powder Technol. 26 (2015) 650–656.

[56] V. Uskoković, D.P. Uskoković, Nanosized hydroxyapatite and other calcium phosphates: chemistry of formation and application as drug and gene delivery agents, J. Biomed. Mater. Res. B: Appl. Biomater. 96B (1) (2011) 152–191.

[57] V. Uskoković, S. Marković, L. Veselinović, S. Škapin, N. Ignjatović, D.P. Uskoković, Insights into the kinetics of thermally induced crystallization of amorphous calcium phosphate, Phys. Chem. Chem. Phys. 20 (2018) 29221–29235.

[58] H. Madupalli, B. Pavan, M.M.J. Tecklenburg, Carbonate substitution in the mineral component of bone: discriminating the structural changes, simultaneously imposed by carbonate in A and B sites of apatite, J. Solid State Chem. 255 (2017) 27–35.